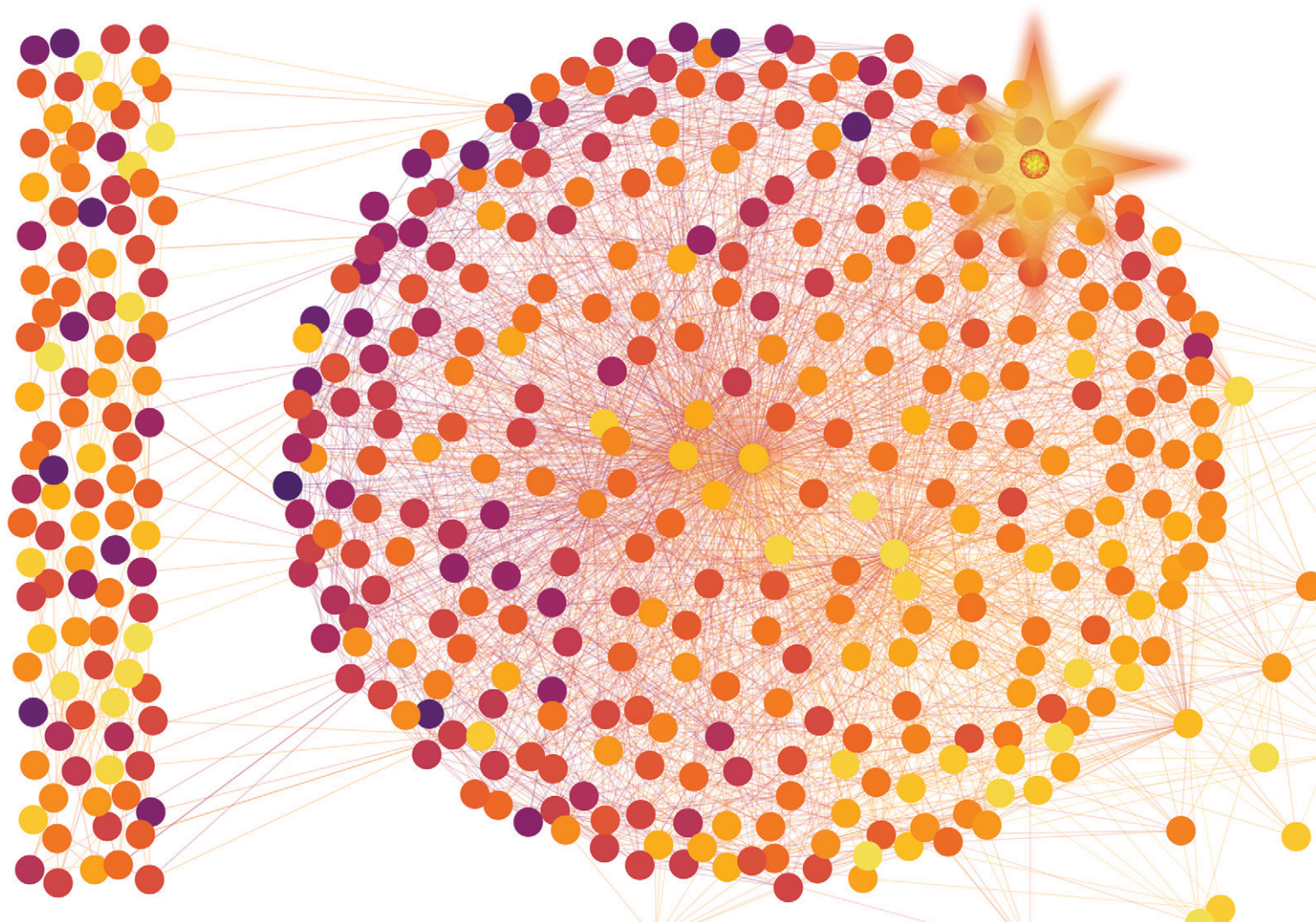


# Catalysis Science & Technology

Volume 12  
Number 2  
21 January 2022  
Pages 341–710

[rsc.li/catalysis](https://rsc.li/catalysis)







Themed collection: Catalysis Science & Technology 10th Anniversary Perspectives

ISSN 2044-4761

**PAPER**

Boon Siang Yeo, Javier Pérez-Ramírez, Núria López *et al.*  
Mechanistic routes toward C<sub>3</sub> products in copper-catalysed  
CO<sub>2</sub> electroreduction

## PAPER

[View Article Online](#)  
[View Journal](#) | [View Issue](#)Cite this: *Catal. Sci. Technol.*, 2022,  
12, 409Mechanistic routes toward C<sub>3</sub> products in copper-catalysed CO<sub>2</sub> electroreduction†Sergio Pablo-García, <sup>‡a</sup> Florentine L. P. Veenstra,<sup>‡b</sup> Louisa Rui Lin Ting, <sup>‡cd</sup>  
Rodrigo García-Muelas, <sup>a</sup> Federico Dattila, <sup>a</sup> Antonio J. Martín,<sup>b</sup>  
Boon Siang Yeo, <sup>\*cd</sup> Javier Pérez-Ramírez <sup>\*b</sup> and Núria López <sup>\*a</sup>

The electrocatalytic CO<sub>2</sub> reduction (eCO<sub>2</sub>R) reaction powered by renewable electricity holds promise for the sustainable production of multi-carbon chemicals and fuels. On Cu-based catalysts, ethylene and ethanol (C<sub>2</sub>) have been produced in appreciable amounts. C<sub>3</sub> products (mostly terminal oxygenates) have limited yields, whereas propylene is puzzlingly absent. Herein, we devise a divide-and-conquer strategy to explain the formation of the C<sub>3</sub>-backbone and elucidate the mechanism responsible for the observed selectivity by combining network graphs, density functional theory, and experiments to prune the network and benchmark the identified path. Our approach concludes that the most frequently reported products, propionaldehyde and 1-propanol, originate from the coupling of CH<sub>2</sub>CH with C(H)O. While propylene and 1-propanol share common intermediates, the former is barely produced due to the unfavourable formation of allyl alkoxy (CH<sub>2</sub>CHCH<sub>2</sub>O), whose crucial nature was confirmed experimentally. This work paves the way for tailoring selective routes towards C<sub>3</sub> products via eCO<sub>2</sub>R.

Received 8th August 2021,  
Accepted 5th December 2021

DOI: 10.1039/d1cy01423d

[rsc.li/catalysis](http://rsc.li/catalysis)

## Introduction

Developing functional catalysts for the electrochemical CO<sub>2</sub> reduction (eCO<sub>2</sub>R) to complex products lies at the core of new efforts to develop sustainable technologies.<sup>1</sup> Among available materials, copper-based electrocatalysts occupy a pivotal role due to their ability to form the C<sub>2+</sub> backbone for high-value fuels and commodity chemicals.<sup>1,2</sup> The type and amount of products formed are sensitive to the applied potential, electrolyte, and the preparation protocol of Cu.<sup>3–6</sup> The established mechanism to the C<sub>2</sub> fraction advocates that CO<sub>2</sub> first reduces to CO, which dimerises to OCCO<sup>–</sup> and subsequently reduces to hydrocarbons and alcohols. Typically, the main C<sub>2</sub> product is ethylene (up to *ca.* 74% Faradaic efficiency FE),<sup>7</sup> although an exceptional ethanol selectivity (*ca.*

91% FE)<sup>8</sup> has been reported on Cu clusters. For C<sub>4</sub> products, the aldol condensation of acetaldehyde (C<sub>2</sub>) gives crotonaldehyde, which reduces to 1-butanol, albeit with low yields.<sup>9</sup> Among C<sub>3</sub> compounds, 1-propanol can be produced with appreciable yields (~23% FE),<sup>10,11</sup> whereas propylene (the corresponding C<sub>3</sub> olefin; 0.36 eV less stable than 1-propanol, Table S1†) has only been detected as a trace product (<0.1% FE).<sup>9</sup> This puzzling outcome contrasts with the vast formation of ethylene, which is less stable than ethanol by 0.47 eV, Table S1.† Furthermore, 2-propanol, which is the most thermodynamically stable C<sub>3</sub> alcohol (0.17 eV lower than 1-propanol, Table S1†), has never been observed in eCO<sub>2</sub>R.<sup>12</sup> Reports have indicated that the formation of the C<sub>3</sub> backbone at high CO concentrations and relatively mild applied potentials (–0.36 to –0.56 V vs. RHE)<sup>11,13</sup> requires asymmetric sites on oxide-derived Cu (OD-Cu) catalysts. Nonetheless, the reasons behind the low selectivity to C<sub>3</sub> products in eCO<sub>2</sub>R at a molecular level is very limited. This is due to the large number of elementary steps (>10<sup>3</sup>) that prevent the use of standard reaction sampling tools based on explicit density functional theory (DFT) and reaction profile analysis.

Herein, we analyse electrocatalytic routes towards C<sub>3</sub> products through a divide-and-conquer strategy based on the generation of the network graph and computational reaction profiles combined with key electrochemical experiments involving C<sub>1</sub>, C<sub>2</sub>, and C<sub>3</sub> reagents. This new methodological approach enables us to (i) identify the most likely C<sub>1</sub>–C<sub>2</sub>

<sup>a</sup> Institute of Chemical Research of Catalonia, ICIQ, The Barcelona Institute of Science and Technology, Av. Països Catalans 16, 43007 Tarragona, Spain. E-mail: [nlopez@iciq.es](mailto:nlopez@iciq.es)

<sup>b</sup> Institute for Chemical and Bioengineering, Department of Chemistry and Applied Biosciences, ETH Zürich, Vladimir-Prelog-Weg 1, 8093 Zürich, Switzerland. E-mail: [jpr@chem.ethz.ch](mailto:jpr@chem.ethz.ch)

<sup>c</sup> Department of Chemistry, National University of Singapore, 3 Science Drive 3, 117543, Singapore. E-mail: [chmyeos@nus.edu.sg](mailto:chmyeos@nus.edu.sg)

<sup>d</sup> Solar Energy Research Institute of Singapore, National University of Singapore, 7 Engineering Drive 1, 117574, Singapore

† Electronic supplementary information (ESI) available: Experimental and computational details, supplementary notes, figures, and tables. See DOI: 10.1039/d1cy01423d

‡ These authors contributed equally to this work.



coupling steps towards  $C_3$  intermediates; (ii) elucidate the bifurcation points to different  $C_3$  products; and (iii) pinpoint kinetic bottlenecks hindering propylene production.

## Experimental and computational methods

The electrocatalytic reactor used for our experiments is a gas-tight cell consisting of two compartments separated by a Nafion 211 membrane with gas-flow inlet and outlet ports. The cell has an OD-Cu working electrode, a gas diffusion layer (GDL) carbon paper counter electrode, and a leak-free Ag/AgCl (3 M KCl) reference electrode. Triplicate measurements were done, with the average values and standard deviations presented in the ESI.† Extended details about reagents, catalysts preparation, electrochemical measurements, detection limits, and product analyses are shown in Experimental and computational details in the ESI.† The OD-Cu catalyst was obtained from CuO (see Fig. S1† for XRD analysis). The physicochemical and catalytic properties of this material have been discussed elsewhere.<sup>9,14</sup>

We initially reduced  $CO_2$  in 0.1 M  $KHCO_3$  at  $-0.95$  V vs. RHE to maximise the production of multi-carbon products,<sup>14</sup> as shown in Fig. 1 (see Fig. S2† for polarisation curves).  $C_1$  and  $C_2$  products account for 53% of the FE, whereas 7% corresponds to  $C_3$  products and the balance is  $H_2$ . Our observed product distribution agrees with selectivity trends presented in the literature, which are summarised in Fig. S3,† and the paths to  $C_2$  products are shown in Fig. S4–S5.† To unravel the selectivity patterns observed from both the literature and our experiments, our workflow entails: (i) building the reaction network by encoding the corresponding structural graphs; (ii) sampling the intermediates by DFT; (iii) computing all  $C_1$ – $C_2$  backbone couplings by DFT; (iv) pruning the network of non-viable backbone formation routes by probing the products from CO, formaldehyde, and methanol co-reduction with  $C_2$

reactants (Table 1), with particular attention to missing products; (v) computing all routes from the  $C_3$  backbone to the final products using DFT and linear-scaling relationships (Table S15†) to identify the best routes towards propanol and propylene; (vi) experimental benchmarking of the main predicted routes *via* electrocatalytic tests with key intermediates.

While the routes to  $C_1$  and  $C_2$  products can be probed manually, as shown in the literature,<sup>15–20</sup> the analysis of routes to  $C_3$  products demands automation. The full network containing all  $C_1$ ,  $C_2$ , and  $C_3$  intermediates has 463 elements, represented here as nodes in a graph (see “Graph representation of the reaction network” in Experimental and computational details). The energies of intermediates (referenced to  $CO_2$ ,  $H_2O$ , and  $H_2$ ) were evaluated with the computational hydrogen electrode (CHE)<sup>21,22</sup> containing the DFT energy obtained with a PBE-D2 formulation<sup>23–25</sup> (corrected for metal overbinding), our in-house developed implicit solvation model,<sup>26,27</sup> and the polarisation term<sup>9,28</sup> (see eqn S1–S4† in the Experimental and computational details). The D2 contribution on  $H^*$  and  $CO^*$  adsorption is small: 0.04 and 0.14 eV, respectively. Intermediates are linked by 2266 steps (edges linking the nodes in the graph): 55  $C_1$ – $C_1$  and 636  $C_1$ – $C_2$  couplings, 683 C–H and 305 O–H hydrogenations, and 587 C–O(H) cleavages. To ensure the desired accuracy, 586 out of all  $C_1$ – $C_2$  couplings (Tables S16–S19,† 92% of total), 10 C–O(H) breakings (Table S20†), and 8 hydrogenations (Table S21†) were explicitly obtained *via* nudged elastic band (DFT-NEB)<sup>29</sup> and confirmed by vibrational analysis. Initial guesses for NEB were generated automatically (Experimental and computational details in ESI† and Notes S1–S4). Linear scaling relationships (LSR) were employed in the initial fast-sampling of C–H and O–H hydrogenations as they are reliable for these cases<sup>20,30,31</sup> (Table S15†). The transition states for key hydrogenation steps in the main path were further refined with DFT-NEB. Heyrovsky-type reactions for C–OH breakings and C–H formations were considered (Note S5†). Tests on density functionals, LSR, and charge analysis are described in Note S6 and Fig. S6–S9,† and demonstrate that our strategy provides an excellent cost-efficiency balance.

Benchmark electrochemical experiments (Table 1) involving the reduction of selected  $C_1$  and  $C_2$  compounds and their mixtures were conducted at mild overpotentials ( $-0.4$  V vs. RHE) in alkaline pH, where the production of multi-carbon products is expected to be boosted.<sup>32,33</sup> In the case of aldehydes, which undergo side reactions in alkaline media,<sup>9</sup> electrolysis was performed in neutral potassium phosphate buffer (PPB) at  $-1.0$  V vs. RHE as the optimum condition for the production of propylene (Table S3†). To avoid interference of the parasitic hydrogen evolution reaction (HER) in assessing reactivity, we compared production rates, instead of Faradaic efficiencies, of the carbonaceous products formed under different conditions. Additional information on the experimental conditions can be found in Note S7.†

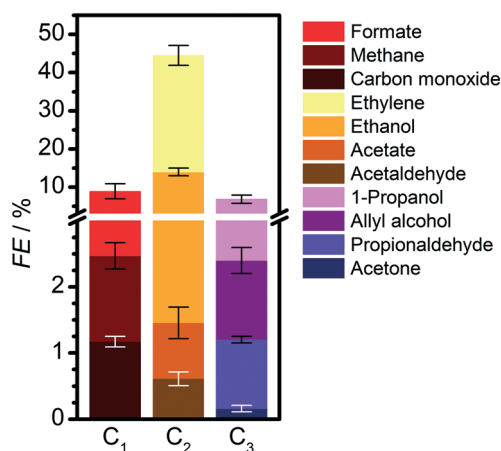



Fig. 1  $C_1$ – $C_3$  products formed from the electrocatalytic  $CO_2$  reduction on oxide-derived copper in 0.1 M  $KHCO_3$  at  $-0.95$  V vs. RHE. Detailed results are presented in Table S2.† Hydrogen FE is 37.4%.



**Table 1** Summary of C<sub>3</sub> products and their corresponding formation rates observed experimentally from the electrolysis of C<sub>1</sub> or a mixture of C<sub>1</sub> and C<sub>2</sub> compounds on OD-Cu. The C<sub>1</sub> and C<sub>2</sub> compounds used are listed in the topmost row and leftmost column respectively, while the experimental conditions are indicated in the footnotes. A colour code has been added to highlight the higher C<sub>3</sub> formation rates. For reference, the formation rates of C<sub>3</sub> products from eCO<sub>2</sub>R are given in parenthesis, coloured scale is indicated in the lower bar. The full set of experiments and product distributions are shown in Tables S2–S14†

| C <sub>2</sub> \ C <sub>1</sub>                       | Carbon monoxide, CO   | Formaldehyde, CH <sub>2</sub> O                                  | Methanol, CH <sub>3</sub> OH   | Carbon dioxide, CO <sub>2</sub>  |
|---|---|--|--------------------------------|--|
| No C <sub>2</sub>                                     | 1-Propanol (0.02) <sup>A</sup><br>1-Propanol (2.2) <sup>B</sup><br>Allyl alcohol (2.1) <sup>B</sup><br>Propionaldehyde (0.4) <sup>B</sup> | No C <sub>3</sub> <sup>A,B</sup>                                 | No C <sub>3</sub> <sup>A</sup> | 1-Propanol (75.8) <sup>C</sup><br>Allyl alcohol (25.2) <sup>C</sup><br>Propionaldehyde (20.3) <sup>C</sup><br>Acetone (3.2) <sup>C</sup> |
| Oxalate, C <sub>2</sub> O <sub>4</sub>                | 1-Propanol (0.4) <sup>A</sup>   | No C <sub>3</sub> <sup>A</sup>                                   | 1-Propanol (0.1) <sup>A</sup>  | X  |
| Glyoxal, CHOCHO                                       | 1-Propanol (0.3) <sup>A</sup>   | No C <sub>3</sub> <sup>A</sup>                                   | 1-Propanol (0.1) <sup>A</sup>  | X  |
| Acetate, CH <sub>3</sub> COO <sup>−</sup>             | 1-Propanol (0.2) <sup>A</sup>   | No C <sub>3</sub> <sup>A</sup>                                   | No C <sub>3</sub> <sup>A</sup> | X  |
| Ethylene glycol, CH <sub>2</sub> OHCH <sub>2</sub> OH | 1-Propanol (0.5) <sup>A</sup>   | No C <sub>3</sub> <sup>A</sup>                                   | No C <sub>3</sub> <sup>A</sup> | X  |
| Ethanol, CH <sub>3</sub> CH <sub>2</sub> OH           | 1-Propanol (0.2) <sup>A</sup>   | No C <sub>3</sub> <sup>A</sup>                                   | No C <sub>3</sub> <sup>A</sup> | X  |
| Acetaldehyde, CH <sub>3</sub> CHO                     | 1-Propanol (12.1) <sup>B</sup><br>Propylene (trace) <sup>B</sup>  | Propylene (1.4) <sup>B</sup><br>Allyl alcohol (2.0) <sup>B</sup> | X                              | X  |

<sup>A</sup> 0.1 M KOH at −0.40 V vs. RHE  
<sup>B</sup> 0.1 M PPB at −1.00 V vs. RHE  
<sup>C</sup> 0.1 M KHCO<sub>3</sub> at −0.95 V vs. RHE  
<sup>X</sup> Not performed

lower  higher  
 rate / μmol cm<sup>−2</sup> h<sup>−1</sup>

## Results and discussion

### Routes to main C<sub>1</sub> and C<sub>2</sub> products and precursors

The main outcome of previous computational studies on the manually-analysed network for eCO<sub>2</sub>R to C<sub>1</sub> and C<sub>2</sub> products over Cu(111) or Cu(100) can be summarised as follows:<sup>15–20</sup> CO<sub>2</sub> adsorbs on the metal and reduces to CO, a precursor for methanol and methane (C<sub>1</sub>). Alternatively, CO dimerises to OCCO<sup>−</sup>, which has been claimed to be the rate-determining step in the formation of the C<sub>2</sub> backbone.<sup>15–19</sup> On Cu(100), this process is endergonic by 0.84 eV at −0.4 V vs. RHE, (with an activation barrier of 1.42 eV), but can be promoted on defective surfaces.<sup>34</sup> Additionally, OCCO<sup>−</sup> can be stabilised by electrolyte cations<sup>35,36</sup> and the electric field at the cathode.<sup>28,36,37</sup> OCCO<sup>−</sup> is further protonated and then dehydrated to CCO upon a proton-coupled electron transfer step. The latter intermediate is subsequently hydrogenated to CH<sub>2</sub>CHO.<sup>1,38</sup> If hydrogenolysis occurs on the remaining O atom, CH<sub>2</sub>CH is formed, leading to ethylene. If hydrogenation occurs on the α-C (C<sub>α</sub>H<sub>2</sub>CHO), ethanol is formed (Fig. S4 and S5†).

### Exploring C<sub>1</sub>–C<sub>2</sub> coupling reactions

To unravel the most likely reaction routes towards C<sub>3</sub> backbone formation, a sequential analysis combining available reports, experiments and theory was applied. The possible C<sub>1</sub>–C<sub>2</sub> couplings shown in Fig. 2a and Tables S16–S18† emerge from combining 10 C<sub>1</sub> (−CH<sub>x</sub>O\* or −CH<sub>x</sub>\*) and 70 C<sub>2</sub> precursors that can be hydrocarbons (CH<sub>y</sub>CH<sub>z</sub>\*−) or

oxygenates (CH<sub>y</sub>OCH<sub>z</sub>O\*−, CH<sub>y</sub>OCH<sub>z</sub>\*−, CH<sub>y</sub>CH<sub>z</sub>O\*−). This gives rise to oxygenate-to-oxygenate, hydrocarbon-to-oxygenate, and hydrocarbon-to-hydrocarbon C–C coupling reactions. Thus, six families of intermediates, namely C<sub>3</sub>H<sub>x</sub>, 1-C<sub>3</sub>OH<sub>x</sub>, 1,3-C<sub>3</sub>O<sub>2</sub>H<sub>x</sub>, 2-C<sub>3</sub>OH<sub>x</sub>, 1,2-C<sub>3</sub>O<sub>2</sub>H<sub>x</sub> and 1,2,3-C<sub>3</sub>O<sub>3</sub>H<sub>x</sub>, *x* = 0–8 (families 1–6 in Fig. 2a) are formed, where the prefix numbers show the position of the oxygenated functional group, irrespective of it having alcohol, alkoxy, aldehyde, or ketone character. Molecular fragments with carboxylate, carboxylic acid, ethers, or cyclic backbones were not considered, as these functionalities have not been found experimentally in the pool of C<sub>3</sub> products.

We then compared the C<sub>3</sub> products formed from the electrolysis of mixtures of CO with different C<sub>2</sub> molecules (glyoxal, ethylene glycol, oxalate, acetate, ethanol, acetaldehyde) at open-circuit potential and −0.4 and −1.0 V vs. RHE (Tables 1 and S6 and S8–S9†). At −0.4 V vs. RHE, all these mixtures generate 1-propanol at rates much larger than the reduction of CO alone (Table S4†). Mixtures with ethylene glycol gave the highest yield, while those with ethanol and acetate gave the lowest. Propylene was not detected (detection limits of gaseous products are equivalent to 0.5 μmol cm<sup>−2</sup> h<sup>−1</sup>, see ESI† Experimental and computational details). Overall, if a set of products with a given C<sub>x</sub>O<sub>y</sub> backbone is not observed experimentally, then such couplings can be considered unlikely, and the routes pruned from the network.

To further verify the nature of the active C<sub>1</sub> fragment leading to 1-propanol, electrocatalytic tests of the C<sub>2</sub>



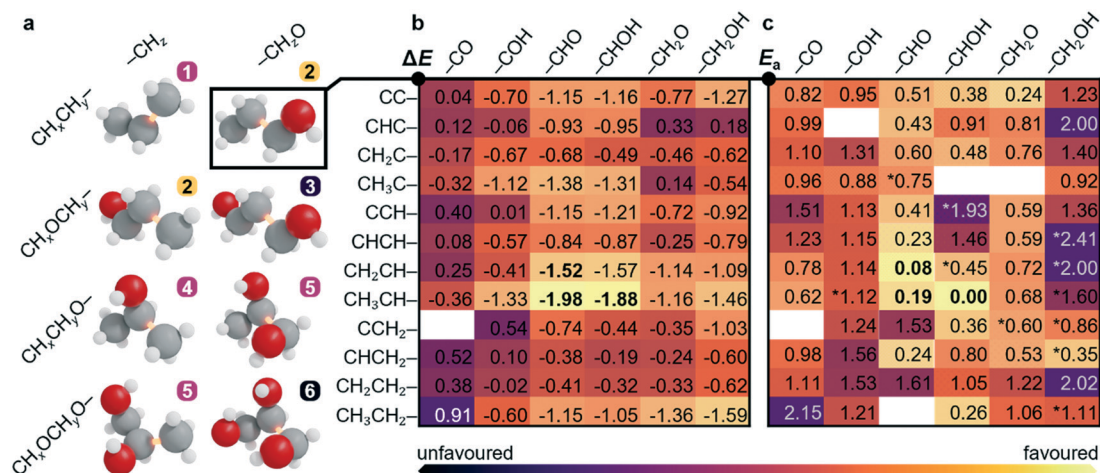


**Fig. 2** Screening process to narrow down the  $C_1$ - $C_2$  coupling steps. a  $C_xH_yO_z$  backbones that can be obtained through  $C_1$ - $C_2$  couplings. Only the fully hydrogenated product is shown with the bond formed marked in orange. The numbers label six families of molecules and the colour stands for their abundance reported from  $CO_2$  reduction experiments, found either from the literature or this work. High, low, or zero relative abundance is shown in orange, purple, and black, respectively. Backbones 3 and 5 can be formed from two combinations of  $C_1$  and  $C_2$  intermediates. b and c Reaction and activation energies for  $CH_xCH_y-CH_2O$  couplings between a  $C_1$  oxygenate and a  $C_2$  hydrocarbon,  $\Delta E$  and  $E_a$  in eqn S3-S6.† Most likely steps indicated in bold. The full set of  $10 C_1 \times 70 C_2$  coupling reactions is shown in Tables S16-S18.† Further details can be found in Notes S1-S2 and S8-S9.†

compounds with either methanol or formaldehyde (Table 1) were conducted. 1-Propanol was not detected in some of these experiments, though we observed allyl alcohol and propylene from the electrolysis of a formaldehyde and acetaldehyde mixture. Moreover, the reduction of  $CH_2O$  itself produced only  $CH_3OH$  and  $CH_4$  (Table 1 and S4†), but it does not produce  $C_2$  and  $C_3$  compounds as it is hardly broken into the more reactive  $CH_2$  and  $CHO$  species (Table S22†).  $CH_3OH$ , on the other hand, was electrochemically inert (Tables S12 and S13†). The unique predominance of 1-propanol in experiments using  $CO$  indicates that  $*CO$  (or a derivative like  $*CHO$ ) is instrumental in promoting 1-propanol formation. This is further confirmed by the absence of 1-propanol in experiments starting with  $CH_2O$  or  $CH_3OH$  (Table 1).

After considering the experimental input, we then switched to theory to explore the  $C_1$ - $C_2$  coupling reactions based on the reaction energies ( $\Delta E$ , Table S16†), activation energies obtained by DFT-NEB ( $E_a$ , Table S17†), and complemented by the electrochemical driving force computed as the polarisation variation upon reaction ( $\Delta\Delta Q_B$  in eqn S6, Table S18†). More favourable values are shown in brighter colours in Fig. 2b and c. The most likely candidates were then selected among all couplings, which reduced the set to  $CH_2CH-CHO$  and  $CH_3CH-CHO$ . In the following paragraphs, we describe how the different coupling families are retained or discarded during the analysis of the network based on abovementioned literature, experimental, and theoretical analyses:

**1,2,3- $C_3O_3H_x$  backbone.** Early computational studies proposed that the  $C_3$  backbone was formed *via* trimerisation of  $*CO$ <sup>39,40</sup> (family 6 in Fig. 2a, 1,2,3- $C_3O_3H_x$ ). We computed this potential reaction and found a relatively high activation barrier of  $E_a = 0.96$  eV. Furthermore, the  $CO$ -trimer reverts

$0.14 e^-$  to the surface, so the net reaction is therefore expected to be hindered under reductive potentials (Table S19†). Alternatively, a sequential process can be envisaged where  $CO$  dimerises to  $OCCO^-$ , which further reacts with  $CHO$  ( $E_a = 0.73$  eV,  $\Delta\Delta Q_B = -0.81 e^-$ ), or  $COCHO$  with  $CO$  ( $E_a = 0.78$  eV,  $\Delta\Delta Q_B = -0.39 e^-$ ) to form  $COCOCO$  as the base of the 1,2,3- $C_3O_3H_x$  backbone. Only the latter reaction would be promoted at more reducing potentials. However, should this reaction occur, glycerol would likely appear as a product of  $CO_2$  reduction, but this has not been reported in the literature. Thus, the absence of glycerol as a product combined with the medium to high computed barriers and electrochemical penalties suggest that 1,2,3- $C_3O_3H_x$  (6 in Fig. 2a) intermediates are unlikely to participate in the main mechanistic route.

**1,2- $C_3O_2H_x$  and 1,3- $C_3O_2H_x$  backbones.** There are two families of  $C_3O_2H_x$  intermediates, with O atoms in different positions: 1,2- $C_3O_2H_x$  (5) and 1,3- $C_3O_2H_x$  (3, Fig. 2a). Among the products derived from 1,2- $C_3O_2H_x$ , only 1-hydroxyacetone has been reported in the literature, albeit in trace quantities.<sup>2</sup> Indeed, some  $CH_xCH_yO^*-CH_2O^*$  pairs have low coupling barriers, such as the coupling of  $CH_2CO$ ,  $CH_3CO$ , and  $CH_3COH$  with  $CHO$  (up to 0.32 eV, Table S17†). Remarkably, the  $CHO$  coupling is expected to be strongly promoted under reductive potentials ( $\Delta\Delta Q_B = -0.52 e^-$ , Table S18†). However, these  $C_2$  intermediates have higher potential energies than other structural isomers (Fig. S5†). As such, their concentration is expected to be too low at  $-0.4$  V vs. RHE to form any significant amount of 1,2- $C_3O_2H_x$  products, as confirmed by the range of products observed in our experiments (Tables S8-S13†). The formation of 1,3- $C_3O_2H_x$  products is expected to proceed from  $CH_2OCH-CHO(H)$  ( $E_a \leq 0.34$  eV) or  $CH_2OHCH-CHO$  ( $E_a < 0.16$  eV). These reactions





would occur as chemical steps and are not favoured under  $e\text{CO}_2\text{R}$  conditions (according to computational charge considerations, Table S18†). Our simulation results may also explain why 1,3- $\text{C}_3\text{O}_2\text{H}_x$  products (*viz.* 1,3-propanediol and 3-hydroxypropanal) have not been experimentally observed for Cu-based catalysts.

**2- $\text{C}_3\text{OH}_x$  backbone via  $\text{H}_x\text{C}_1\text{-C}_2\text{H}_y\text{O}$  coupling.** We are now left with the paths that generate mono-oxygenated  $\text{C}_3$  intermediates. 2- $\text{C}_3\text{OH}_x$  products can be produced from the coupling of a  $\text{CH}_x\text{CH}_y\text{O}^*$  fragment, such as  $\text{CH}_3\text{CHO}^*$  and  $\text{CH}_2\text{CHO}^*$ , with a  $\text{C}_1$  hydrocarbon,  $-\text{CH}_x^*$  (family 4 in Fig. 2a, Tables S16–S18†). This pathway may expectedly yield 2-propanol, which is 0.17 eV more stable than 1-propanol (Table S1†), whereas intermediates leading to these two species show similar stabilities (Fig. S10†). However, 2-propanol was not experimentally detected (Table 1). Previous experiments on Cu-based catalysts have only detected small amounts of acetone,<sup>2</sup> in line with our present results (0.2% FE, Fig. 1, Table S2†). Acetone is likely produced by coupling  $\text{CH}_3\text{CO}$  with  $\text{CH}_2$ , ( $\Delta E = -1.57$  eV;  $E_a = 0.28$  eV) and the further hydrogenation of the unsaturated aliphatic carbon atom.

**1- $\text{C}_3\text{OH}_x$  backbone.** Most of the  $\text{C}_3$  products detected in our experiments belong to the 1- $\text{C}_3\text{OH}_x$  family (2 in Fig. 2a), namely 1-propanol ( $\text{CH}_3\text{CH}_2\text{CH}_2\text{OH}$ , 1- $\text{C}_3\text{OH}_8$ ), with propionaldehyde and allyl alcohol ( $\text{CH}_3\text{CH}_2\text{CHO}$  and  $\text{CH}_2\text{-CHCH}_2\text{OH}$ , 1- $\text{C}_3\text{OH}_6$ ) produced at smaller rates (Table 1).<sup>2,41</sup> Considering the experimentally observed scarcity of  $\text{C}_3\text{O}_2\text{H}_x$  and  $\text{C}_3\text{O}_3\text{H}_x$  products, we infer that there is only one oxygen atom present during the coupling, either on the  $\text{C}_1$  or the  $\text{C}_2$  moiety. Reported experiments<sup>42–45</sup> show that during  $e\text{CO}_2\text{R}$ , the maximum production of 1-propanol occurs when high amounts of CO and  $\text{C}_2\text{H}_4$  are formed simultaneously. Indeed, the lowest activation barriers are found for the highly exothermic  $\text{CH}_2\text{CH-CHO}$  and  $\text{CH}_3\text{CH-CHO(H)}$  couplings ( $\Delta E < -1.50$  eV,  $E_a \leq 0.19$  eV, Fig. 2b and c). As  $\text{CH}_2\text{CH}$  is a precursor of  $\text{C}_2\text{H}_4$ , and  $\text{CHO(H)}$  is directly formed from CO, we conclude that all such paths are highly likely. Couplings involving  $\text{C}_2$  moieties less hydrogenated than  $\text{CH}_2\text{CH}$  or  $\text{CH}_2\text{-CHO}$  (another  $\text{C}_2\text{H}_4$  precursor) are therefore less likely. In the remaining region, most  $\text{C}_1\text{-C}_2$  couplings are highly activated (Fig. 2c). Thus,  $\text{CH}_2\text{CHCHO}^*$  and  $\text{CH}_3\text{CHCHO}^*$  intermediates are common precursors for  $\text{C}_3$  products. To a lesser degree,  $\text{CH}_2\text{CHCO}^*$  can also be formed if the coupling starts with  $-\text{CO}$  instead of  $-\text{CHO}$ , Fig. 3. Finally, reactions involving  $\text{C}_2$  oxygenated precursors (Tables S16–S18†) have higher barriers, such as the  $\text{CH}_2\text{-CCH}_2\text{O}$  coupling (while the process is exothermic,  $\Delta E = -1.61$  eV, it exhibits a non negligible activation barrier,  $E_a = 0.39$  eV). Upon reaction, part of the electronic density of  $\text{CH}_2\text{CHCHO}^*$  is returned to the surface ( $-0.30$  e<sup>-</sup>, Table S18†). The reaction is therefore unfavoured at strongly reductive potentials, which explains the decrease in 1-propanol production as the potential becomes more negative.<sup>1,2</sup>

The activation barriers of the transition states associated with the formation of key  $\text{C}_3$  intermediates are sensitive to

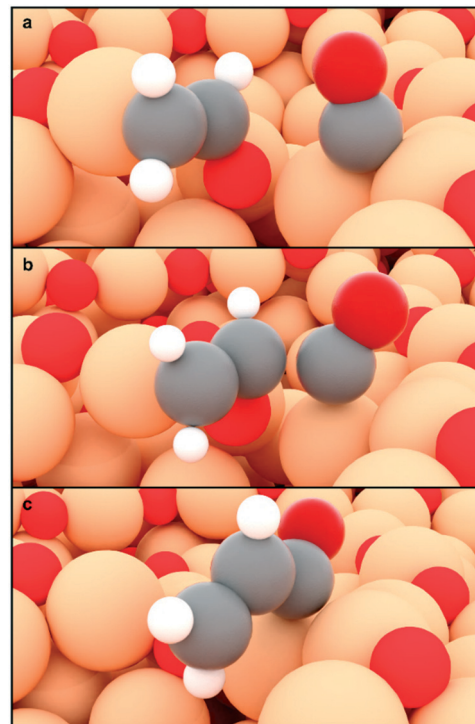


**Fig. 3**  $\text{CH}_2\text{CHO-CO}$  coupling on OD-Cu models.<sup>34</sup> a–c Initial, transition, and final state respectively. A surface cavity with high oxygen affinity assists the C–O bond breaking of the  $\text{CH}_2\text{CHO}^*$  precursor. A neighbouring polarised site,  $\text{Cu}^{\delta+}$ , weakly adsorbs CO.

surface geometry and ensembles. Since defective Cu surfaces have been reported as selective to propanol formation,<sup>39,44</sup> we assessed the role of defects on OD-Cu models<sup>34</sup> for the concerted coupling of  $\text{CH}_2\text{CH(O)}^*\text{-CO}^*$  to yield the simplest  $\text{C}_3$  precursor,  $\text{CH}_2\text{CHCO}$ , Fig. 3. The Cu and  $\text{CuO}_x$  structures were optimised for 10 ps through *ab initio* molecular dynamics and recurrent morphological motifs occurred upon surface reconstruction.<sup>34</sup> Out of twelve surface motifs assessed (Fig. S11†),<sup>34,46</sup> an active site consisting of a surface cavity (Fig. 3a, centre) and a neighbouring  $\text{Cu}^{\delta+}$  atom (Fig. 3a, right) is the most suitable for promoting the coupling. While  $\text{CH}_2\text{CHO}^*$  is trapped at the surface cavity, the high oxygen affinity of this site leads to the breaking of its C–O bond to give  $\text{CH}_2\text{CH}^*$  (Fig. 3b). On the other hand, CO adsorption is almost thermoneutral on the polarised copper site. Thus, the  $\text{CH}_2\text{CH}^*$  fragment can easily couple to the weakly bound  $\text{CO}^*$  to form the  $\text{C}_3$  backbone (exergonic by 0.13 eV; Fig. 3c). In absence of polarized Cu sites (Fig. S11†), this step is endergonic by at least 0.6 eV, thus confirming the instrumental role of surface polarization. This coupling mechanism may explain the high selectivity toward 1-propanol (FE = 23% at  $-0.44$  V vs. RHE) achieved on highly defective Cu surfaces containing a large number of surface cavities.<sup>11,39,44</sup> This concept can also be extended to other key  $\text{C}_1\text{-C}_2$  coupling reactions from moieties directly derived from  $\text{CH}_2\text{CHO}$  and CO, such as  $\text{CH}_2\text{CH-CHO}$  and  $\text{CH}_3\text{CH-CHO}$ . Going beyond pure copper catalysts, we propose that intermetallic alloys containing high oxygen affinity elements coupled with weak CO binding sites could be highly



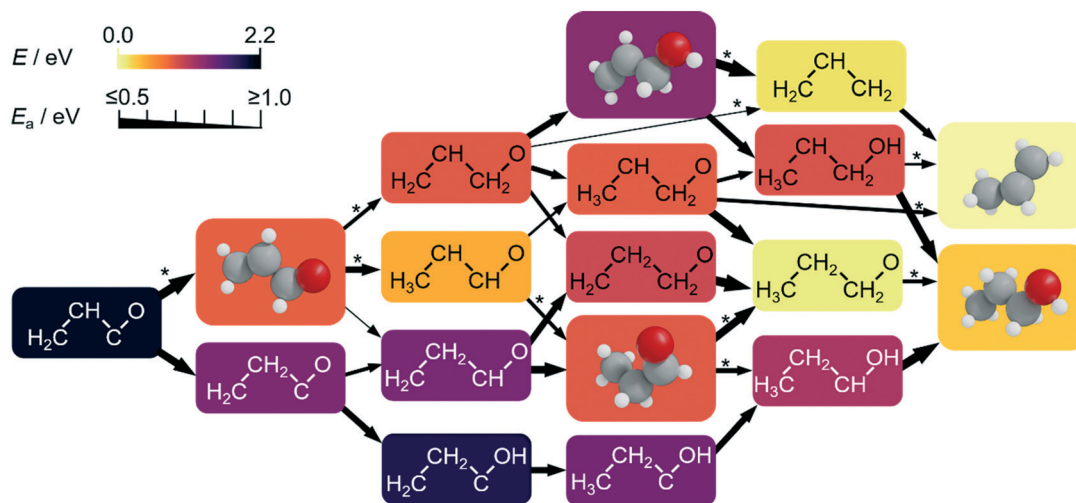


**Fig. 4** Computed subnetwork for  $\text{CH}_2\text{CHCO}$  and  $\text{CH}_2\text{CHCHO}$  conversion to propylene ( $\text{C}_3\text{H}_6$ ) and 1-propanol ( $\text{C}_3\text{H}_7\text{OH}$ ) at  $-0.4$  V vs. RHE (full network in Fig. S12–S14†). The colours of the boxes scale with the relative DFT energy of their intermediates (eqn S3†). Relevant intermediates which can desorb and be used as probe molecules are drawn in 3D. We used allyl alcohol ( $\text{C}_3\text{H}_5\text{OH}$ ) and propionaldehyde ( $\text{C}_3\text{H}_6\text{O}$ ) as reactants in our experiments to confirm the pathways predicted by the network (Tables S23–S24†). The thickness of the arrows connecting the intermediates account for the activation energies ( $E_a$ , obtained by LSR. Those obtained explicitly by DFT are denoted by \*).

selective to  $\text{C}_3$  as well. For instance, Cu–Ag alloys exhibited enhanced propanol selectivity depending on the silver atomic ratio,<sup>13,47</sup> suggesting a CO spillover mechanism<sup>48</sup> from Ag domains to facilitate the formation of  $\text{CH}_2\text{CH-CO}$ .

### Routes to $\text{C}_3$ products

**Routes to 1-propanol.** Once the  $\text{C}_3$  backbone is formed, the  $\text{C}_3$  subnetwork (Fig. 4) starting from  $\text{CH}_2\text{CHCHO}^*$  (orange) and  $\text{CH}_2\text{CHCO}^*$  (black) can be employed to analyse

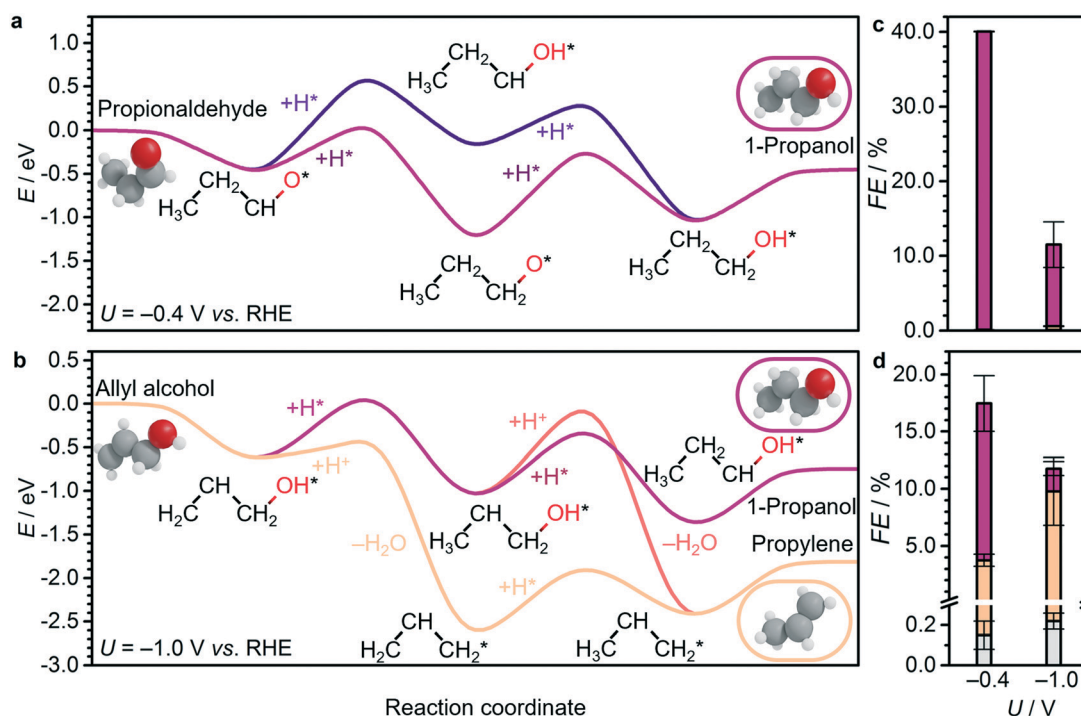


**Fig. 5** a and b Energy profiles for electrocatalytic reduction of key  $\text{C}_3$  compounds on Cu(100), using  $\text{H}_2$ ,  $\text{CO}_2$ , and  $\text{H}_2\text{O}$  as thermodynamic sinks, and shifting the energy reference to make a propionaldehyde and b allyl alcohol the zero. Corresponding products for experimental electroreduction of c propionaldehyde and d allyl alcohol at  $-0.4$  V and  $-1.0$  V vs. RHE on OD-Cu: propane (grey), propylene (orange), and 1-propanol (purple). Full product distributions are shown in Tables S23 and S24†. Other energy profiles at  $0.0$  V,  $-0.4$  V, and  $-1.0$  V vs. RHE are shown in Fig. S15–S17†. The (\*) symbol refers to species adsorbed on the surface. Detailed DFT values can be found in Tables S20–S21†.



selectivity trends. The colour code of the boxes in Fig. 4 represents the computed relative stability of the intermediates (thermodynamics), while the thickness of the lines linking the intermediates accounts for the barriers (thicker lines stand for faster steps). The hydrogenation of  $\text{CH}_2\text{CHCO}^*$  gives  $\text{CH}_2\text{CHCHO}^*$ , which then evolves *via*  $\text{CH}_3\text{CHCHO}^* \rightarrow \text{propionaldehyde} (\text{CH}_3\text{CH}_2\text{CHO}^*) \rightarrow \text{propanoxy} (\text{CH}_3\text{CH}_2\text{CH}_2\text{O}^*) \rightarrow 1\text{-propanol}$ . The existence of this path is confirmed experimentally, since the electrochemical reduction of propionaldehyde on OD-Cu yielded predominantly 1-propanol (Fig. 5c, Table S23†). Alternatively, the 1-propanol formation can proceed through  $\text{CH}_2\text{CH}_2\text{CO}^* \rightarrow \text{CH}_2\text{CH}_2\text{CO}^*\text{H} \rightarrow \text{CH}_3\text{CH}_2\text{COH}^* \rightarrow \text{CH}_3\text{CH}_2\text{CHOH}^* \rightarrow 1\text{-propanol}$  (bottom path in Fig. 4, and 5a).

**Routes to propylene.** Mono-oxygenates can be converted to propylene *via* dehydration reactions starting from  $\text{CH}_2\text{CHCO}(\text{H})^*$ ,  $\text{CH}_2\text{CHCHO}(\text{H})^*$ ,  $\text{CH}_3\text{CHCHO}(\text{H})^*$ ,  $\text{CH}_2\text{CHCH}_2\text{O}(\text{H})^*$ , and  $\text{CH}_3\text{CHCH}_2\text{O}(\text{H})^*$ , where (H) represents an optional hydrogen. The corresponding barriers of these ten reactions were computed (Table S20†). Most C–O(H) bonds are relatively difficult to activate ( $E_a > 1.0$  eV), thus, we depict the ones showing relatively lower barriers ( $\text{CH}_2\text{CHCH}_2\text{O}^*$  and  $\text{CH}_3\text{CHCH}_2\text{O}^*$ ,  $E_a = 0.17$  and  $0.94$  eV, respectively) in Fig. 5a and b. A selectivity switch to propylene occurs when the aldehyde carbon on  $\text{CH}_2\text{CHCHO}^*$  is hydrogenated to form  $\text{CH}_2\text{CHCH}_2\text{O}^*$ , which in turn produces allyl alcohol ( $\text{CH}_2\text{CHCH}_2\text{OH}$ ). To generate propylene, OH is eliminated from the allyl alcohol intermediate, which is then hydrogenated (Fig. 5b). However, this path is not fully selective, as allyl alcohol can also undergo hydrogenation to  $\text{CH}_3\text{CHCH}_2\text{OH}^*$  to form 1-propanol. The C–OH bond breaking in allyl alcohol ( $\text{CH}_2\text{CHCH}_2\text{OH}$ ) has a low barrier of  $0.17$  eV and it is strongly promoted by reducing potentials, with a net charge gain of  $0.87 e^-$  (Table S20† and Fig. 5b).

Therefore, the production of propylene could be traced to the allyl alkoxy ( $\text{CH}_2\text{CHCH}_2\text{O}$ ) intermediate, which is also a direct precursor of allyl alcohol. This proposition was verified experimentally by reducing allyl alcohol on OD-Cu (Fig. 5d), which gave noticeable amounts of propylene as theoretically predicted. Moreover, allyl alcohol ( $1.97 \mu\text{mol cm}^{-2} \text{ h}^{-1}$ ) was detected alongside propylene ( $1.44 \mu\text{mol cm}^{-2} \text{ h}^{-1}$ ) from the reduction of a mixture of acetaldehyde and formaldehyde (Table 1). In this combination, the most likely path occurs when acetaldehyde loses an acidic  $\alpha$ -hydrogen ( $\text{H}_\alpha\text{-CH}_2\text{CHO}$ )<sup>9</sup> to form  $\text{CH}_2\text{CHO}$ , which dehydrates to form  $\text{CH}_2\text{CH}$ . The latter compound reacts with  $\text{CH}_2\text{O}$  to form  $\text{CH}_2\text{CHCH}_2\text{O}^*$  (Fig. 4 and S12–S14†) which is mainly selective towards allyl alcohol and propylene, but not 1-propanol (Table 1). Interestingly, we note that  $\text{CO}_2$  reduction produced 1-propanol ( $FE = 4.4\%$ ) and allyl alcohol ( $FE = 1.2\%$ ) (Fig. 1), while propylene was absent. This can be rationalised by a mild  $\text{eCO}_2\text{R}$  interface alkalisation, which occurs under reaction conditions,<sup>45</sup> favouring the desorption of allyl alkoxy (protonated in solution into allyl alcohol) and thus preventing propylene synthesis. Overall, these observations strongly suggest the key role of allyl alcohol in the route to propylene.

From a broader perspective, the low activity of Cu catalysts for  $\text{eCO}_2\text{R}$  to  $\text{C}_3$  compounds, particularly propylene, could be improved through engineering at different scales. Currently, the most explored approaches to promote multi-carbon products include engineering catalyst surfaces with a high density of defects to improve activity, and optimizing the electrolyte and reactor conditions to alleviate mass transport limitations and tuning the environment at the electrode-electrolyte interface. Modifications at the process level could benefit from three different approaches: (i) one single reactor recycling  $\text{C}_2$  (or  $\text{C}_1$ )  $\text{eCO}_2\text{R}$  products to ensure a high concentration of active intermediates; (ii) independently optimised catalysts and reactors to produce  $\text{C}_1$  (Cu or Ag-based catalysts) and  $\text{C}_2$  (on an oxide-derived Cu catalyst) intermediates, which mix in a third reactor dedicated to the coupling to form the  $\text{C}_3$  backbone or alloys containing close domains of both; (iii) a process able to produce the relevant intermediate allyl alcohol (for which an effective catalyst is not yet known) which is then converted to propylene in a second unit. Although there are some experimental indications in the literature of the potential of strategies (i) and (ii),<sup>13</sup> the detailed understanding of the reaction network and the elucidation of key intermediates presented in this work ultimately serve to direct future works toward realizing these solutions.

## Conclusions

In conclusion, we have performed an integrated mechanistic analysis of the  $\text{eCO}_2\text{R}$  to  $\text{C}_3$  products with all the individual steps available in our open database.<sup>49</sup> Methodological implementations including structural graph network generation, fast energy screenings, and network pruning of irrelevant paths through experimental input allow the effective sampling of the complex  $\text{C}_3$  network pointing out the difficulties found when only a part of the reaction network is sampled.<sup>50</sup>  $\text{C}_2$  and  $\text{C}_3$  products were found to share a common precursor,  $\text{CH}_2\text{CHO}^*$ . Our findings rationalise the generally observed low selectivity of  $\text{eCO}_2\text{R}$  toward  $\text{C}_3$  products, as well as their enhancement on nanostructured Cu catalysts: (i)  $\text{C}_3$  backbones are formed *via* the sluggish coupling of CO or CHO with  $\text{CH}_2\text{CH}^*$ , preferentially at defects and (ii) all  $\text{C}_3$  precursors end up containing at least one O atom, *i.e.*,  $\text{CH}_x + \text{C}_2\text{H}_y$  couplings are highly unlikely. The most stable mono-oxygenated intermediate  $\text{CH}_2\text{CHCHO}^*$  gives access to propylene, propionaldehyde, and 1-propanol. The inaccessible allyl alkoxy intermediate is identified as the most likely kinetic trap preventing propylene production as indicated by simulations and further reinforced with the electrolysis of allyl alcohol leading to propylene. Our mechanistic understanding paves the way towards the development of advanced electrocatalysts that promote  $\text{C}_3$  products, particularly alkenes.

## Author contributions

S. P.-G., Software, methodology, data curation, investigation, visualisation, writing – original draft. F. L. P. V., L. R. L. T.,





Methodology, data curation, investigation, visualisation, writing – original draft. R. G.-M., A. J. M., methodology, data curation, investigation, visualisation, validation, supervision, writing – original draft. F. D., Data curation, investigation, visualisation, writing – review & editing. B. S. Y., J. P.-R., N. L., Conceptualisation, funding acquisition, supervision, project administration, writing – review & editing.

## Conflicts of interest

There are no conflicts of interest to declare.

## Acknowledgements

This work was financed by the Spanish Ministry of Science and Innovation (RTI2018-101394-B-I00, Severo Ochoa Centre of Excellence CEX2019-000925-S 10.13039/501100011033), ETH Research Grant (ETH-47 19-1), the National University of Singapore Flagship Green Energy Program (R143-000-A64-114, R143-000-A55-733 and R143-000-A55-646), and Ministry of Education of Singapore (R143-000-B52-114). This publication was created as part of NCCR Catalysis, a National Centre of Competence in Research funded by the Swiss National Science Foundation. The Barcelona Supercomputing Centre – MareNostrum (BSC-RES) is acknowledged for providing generous computational resources. The authors thank Mavis Pei Lin Kang from NUS for assisting with XRD analyses.

## Notes and references

- 1 S. Nitopi, E. Bertheussen, S. B. Scott, X. Liu, A. K. Engstfeld, S. Horch, B. Seger, I. E. L. Stephens, K. Chan, C. Hahn, J. K. Nørskov, T. F. Jaramillo and I. Chorkendorff, *Chem. Rev.*, 2019, **119**, 7610–7672.
- 2 K. P. Kuhl, E. R. Cave, D. N. Abram and T. F. Jaramillo, *Energy Environ. Sci.*, 2012, **5**, 7050.
- 3 B. Schmid, C. Reller, S. Neubauer, M. Fleischer, R. Dorta and G. Schmid, *Catalysts*, 2017, **7**, 161.
- 4 Y. Kwon, Y. Lum, E. L. Clark, J. W. Ager and A. T. Bell, *ChemElectroChem*, 2016, **3**, 1012–1019.
- 5 X. Wang, A. Xu, F. Li, S. F. Hung, D. H. Nam, C. M. Gabardo, Z. Wang, Y. Xu, A. Ozden, A. S. Rasouli, A. H. Ip, D. Sinton and E. H. Sargent, *J. Am. Chem. Soc.*, 2020, **142**, 3525–3531.
- 6 Y. Y. Birdja, E. Pérez-Gallent, M. C. Figueiredo, A. J. Göttele, F. Calle-Vallejo and M. T. M. Koper, *Nat. Energy*, 2019, **4**, 732–745.
- 7 J. Li, Z. Wang, C. McCallum, Y. Xu, F. Li, Y. Wang, C. M. Gabardo, C. T. Dinh, T. T. Zhuang, L. Wang, J. Y. Howe, Y. Ren, E. H. Sargent and D. Sinton, *Nat. Catal.*, 2019, **2**, 1124–1131.
- 8 H. Xu, D. Rebollar, H. He, L. Chong, Y. Liu, C. Liu, C. J. Sun, T. Li, J. V. Muntean, R. E. Winans, D. J. Liu and T. Xu, *Nat. Energy*, 2020, **5**, 623–632.
- 9 L. R. L. Ting, R. García-Muelas, A. J. Martín, F. L. P. Veenstra, S. T.-J. Chen, Y. Peng, E. Y. X. Per, S. Pablo-García, N. López, J. Pérez-Ramírez and B. S. Yeo, *Angew. Chem., Int. Ed.*, 2020, **59**, 21072–21079.
- 10 D. Gao, I. Sinev, F. Scholten, R. M. Arán-Ais, N. J. Divins, K. Kvashnina, J. Timoshenko and B. Roldan Cuenya, *Angew. Chem., Int. Ed.*, 2019, **58**, 17047–17053.
- 11 J. Li, F. Che, Y. Pang, C. Zou, J. Y. Howe, T. Burdyny, J. P. Edwards, Y. Wang, F. Li, Z. Wang, P. De Luna, C. T. Dinh, T. T. Zhuang, M. I. Saidaminov, S. Cheng, T. Wu, Y. Z. Finck, L. Ma, S. H. Hsieh, Y. S. Liu, G. A. Botton, W. F. Pong, X. Du, J. Guo, T. K. Sham, E. H. Sargent and D. Sinton, *Nat. Commun.*, 2018, **9**, 4614.
- 12 L. Mandal, K. R. Yang, M. R. Motapothula, D. Ren, P. Lobaccaro, A. Patra, M. Sherburne, V. S. Batista, B. S. Yeo, J. W. Ager, J. Martin and T. Venkatesan, *ACS Appl. Mater. Interfaces*, 2018, **10**, 8574–8584.
- 13 X. Wang, Z. Wang, T. T. Zhuang, C. T. Dinh, J. Li, D. H. Nam, F. Li, C. W. Huang, C. S. Tan, Z. Chen, M. Chi, C. M. Gabardo, A. Seifitokaldani, P. Todorović, A. Proppe, Y. Pang, A. R. Kirmani, Y. Wang, A. H. Ip, L. J. Richter, B. Scheffel, A. Xu, S. C. Lo, S. O. Kelley, D. Sinton and E. H. Sargent, *Nat. Commun.*, 2019, **10**, 1–7.
- 14 D. Ren, J. Fong and B. S. Yeo, *Nat. Commun.*, 2018, **9**, 925.
- 15 A. J. Garza, A. T. Bell and M. Head-Gordon, *ACS Catal.*, 2018, **8**, 1490–1499.
- 16 J. D. Goodpaster, A. T. Bell and M. Head-Gordon, *J. Phys. Chem. Lett.*, 2016, **7**, 1471–1477.
- 17 Y. Huang, Y. Chen, T. Cheng, L.-W. Wang and W. A. Goddard, *ACS Energy Lett.*, 2018, **3**, 2983–2988.
- 18 T. Cheng, H. Xiao and W. A. Goddard, *Proc. Natl. Acad. Sci. U. S. A.*, 2017, **114**, 1795–1800.
- 19 Y. Zheng, A. Vasileff, X. Zhou, Y. Jiao, M. Jaroniec and S.-Z. Qiao, *J. Am. Chem. Soc.*, 2019, **141**, 7646–7659.
- 20 Q. Li, R. García-Muelas and N. López, *Nat. Commun.*, 2018, **9**, 526.
- 21 J. K. Nørskov, J. Rossmeisl, A. Logadottir, L. Lindqvist, J. R. Kitchin, T. Bligaard and H. Jónsson, *J. Phys. Chem. B*, 2004, **108**, 17886–17892.
- 22 A. A. Peterson, F. Abild-Pedersen, F. Studt, J. Rossmeisl and J. K. Nørskov, *Energy Environ. Sci.*, 2010, **3**, 1311–1315.
- 23 J. P. Perdew, K. Burke and M. Ernzerhof, *Phys. Rev. Lett.*, 1996, **77**, 3865–3868.
- 24 S. Grimme, *J. Comput. Chem.*, 2006, **27**, 1787–1799.
- 25 N. Almora-Barrios, G. Carchini, P. Błoński and N. López, *J. Chem. Theory Comput.*, 2014, **10**, 5002–5009.
- 26 M. García-Ratés and N. López, *J. Chem. Theory Comput.*, 2016, **12**, 1331–1341.
- 27 M. García-Ratés, R. García-Muelas and N. López, *J. Phys. Chem. C*, 2017, **121**, 13803–13809.
- 28 R. B. Sandberg, J. H. Montoya, K. Chan and J. K. Nørskov, *Surf. Sci.*, 2016, **654**, 56–62.
- 29 G. Henkelman and H. Jónsson, *J. Chem. Phys.*, 2000, **113**, 9978–9985.
- 30 M. García-Mota, B. Bridier, J. Pérez-Ramírez and N. López, *J. Catal.*, 2010, **273**, 92–102.
- 31 S. Pablo-García, M. Álvarez-Moreno and N. López, *Int. J. Quantum Chem.*, 2021, **121**, e26382.
- 32 C. T. Dinh, T. Burdyny, G. Kibria, A. Seifitokaldani, C. M. Gabardo, F. Pelayo García De Arquer, A. Kiani, J. P. Edwards,



- P. De Luna, O. S. Bushuyev, C. Zou, R. Quintero-Bermudez, Y. Pang, D. Sinton and E. H. Sargent, *Science*, 2018, **360**, 783–787.
- 33 J.-J. Lv, M. Jouny, W. Luc, W. Zhu, J.-J. Zhu and F. Jiao, *Adv. Mater.*, 2018, **30**, 1803111.
- 34 F. Dattila, R. García-Muelas and N. López, *ACS Energy Lett.*, 2020, **5**, 3176–3184.
- 35 E. Pérez-Gallent, G. Marcandalli, M. C. Figueiredo, F. Calle-Vallejo and M. T. M. Koper, *J. Am. Chem. Soc.*, 2017, **139**, 16412–16419.
- 36 J. Resasco, L. D. Chen, E. Clark, C. Tsai, C. Hahn, T. F. Jaramillo, K. Chan and A. T. Bell, *J. Am. Chem. Soc.*, 2017, **139**, 11277–11287.
- 37 K. Jiang, R. B. Sandberg, A. J. Akey, X. Liu, D. C. Bell, J. K. Nørskov, K. Chan and H. Wang, *Nat. Catal.*, 2018, **1**, 111–119.
- 38 R. Kortlever, J. Shen, K. J. P. Schouten, F. Calle-Vallejo and M. T. M. Koper, *J. Phys. Chem. Lett.*, 2015, **6**, 4073–4082.
- 39 Y. Pang, J. Li, Z. Wang, C. S. Tan, P. L. Hsieh, T. T. Zhuang, Z. Q. Liang, C. Zou, X. Wang, P. De Luna, J. P. Edwards, Y. Xu, F. Li, C. T. Dinh, M. Zhong, Y. Lou, D. Wu, L. J. Chen, E. H. Sargent and D. Sinton, *Nat. Catal.*, 2019, **2**, 251–258.
- 40 H. Xiao, T. Cheng and W. A. Goddard, *J. Am. Chem. Soc.*, 2017, **139**, 130–136.
- 41 Y. Hori, A. Murata and R. Takahashi, *J. Chem. Soc., Faraday Trans.*, 1989, **85**, 2309–2326.
- 42 Y. Hori, I. Takahashi, O. Koga and N. Hoshi, *J. Phys. Chem. B*, 2002, **106**, 15–17.
- 43 D. Ren, N. T. Wong, A. D. Handoko, Y. Huang and B. S. Yeo, *J. Phys. Chem. Lett.*, 2016, **7**, 20–24.
- 44 T. Zhuang, Y. Pang, Z. Liang, Z. Wang, Y. Li, C. Tan, J. Li, C. T. Dinh, P. De Luna, P. L. Hsieh, T. Burdyny, H. H. Li, M. Liu, Y. Wang, F. Li, A. Proppe, A. Johnston, D. H. Nam, Z. Y. Wu, Y. R. Zheng, A. H. Ip, H. Tan, L. J. Chen, S. H. Yu, S. O. Kelley, D. Sinton and E. H. Sargent, *Nat. Catal.*, 2018, **1**, 946–951.
- 45 F. L. P. Veenstra, N. Ackert, A. J. Martín and J. Pérez-Ramírez, *Chem*, 2020, 1–16.
- 46 F. Dattila, R. García-Muelas and N. López, Dataset associated to: Active and Selective Ensembles in Oxide-Derived Copper Catalysts for CO<sub>2</sub> Reduction, *ioChem-BD*, 2020, DOI: 10.19061/iochem-bd-1-165.
- 47 A. Herzog, A. Bergmann, H. S. Jeon, J. Timoshenko, S. Köhl, C. Rettenmaier, M. Luna Lopez, F. T. Haase and B. Roldan Cuenya, *Angew. Chem., Int. Ed.*, 2021, **60**, 7426–7435.
- 48 P. Iyengar, M. J. Kolb, J. R. Pankhurst, F. Calle-Vallejo and R. Buonsanti, *ACS Catal.*, 2021, **11**, 4456–4463.
- 49 R. García-Muelas, S. Pablo-García and N. López, Dataset associated to: Mechanistic Routes toward C<sub>3</sub> products in Copper-Catalyzed CO<sub>2</sub> Electroreduction, 2020, DOI: 10.19061/iochem-bd-1-175.
- 50 M. T. Tang, H.-J. Peng, J. H. Stenlid and F. Abild-Pedersen, *J. Phys. Chem. C*, 2021, **125**, 26437–26447.

